Perspectives on Proterozoic Surface Ocean Redox From Iodine Contents in Ancient and Recent Carbonate

Iodine constraints on Proterozoic shallow ocean redox and their biological implications

Dalton S. Hardisty[1,2*], Zunli Lu[3], Andrey Bekker[1], Charles W. Diamond[1], Benjamin C. Gill[4], Ganqing Jiang[5], Linda C. Kah[6], Andrew H. Knoll[7], Sean J. Loyd[8], Magdalena R. Osburn[9], Noah J. Planavsky[10], Chunjiang Wang[11], Xiaoli Zhou[3], and Timothy W. Lyons[1]

[1]Department of Earth Sciences, University of California, Riverside, CA USA (*correspondence: dhardisty@whoi.edu)
[2]Department of Geology and Geophysics, Woods Hole Oceanographic Institue, Woods Hole, MA USA
[3]Department of Earth Sciences, Syracuse University, Syracuse, NY USA
[4]Department of Geosciences, Virginia Polytechnic and State University, Blacksburg, VA USA
[5]Department of Geoscience, University of Nevada, Las Vegas, NV USA
[6]Department of Earth and Planetary Sciences, University of Tennessee, Knoxville, TN USA
[7]Department of Earth and Planetary Sciences, Harvard University, Cambridge, MA USA
[8]Department of Geological Sciences, California State University, Fullerton, CA USA
[9]Department of Earth and Planetary Sciences, Northwestern University, Evanston, IL USA
[10]Department of Geology and Geophysics,Yale University, New Haven, CT USA
[11]College of Geosciences, China University of Petroleum, Beijing, China

Key Words: Proterozoic oxygen; Shuram isotope anomaly; carbonate diagenesis; Bahamas; iodine; metazoan evolution

Abstract

Surface ocean oxygen levels during the Proterozoic Eon—the location and time interval hosting the emergence and initial recorded diversification of eukaryotes—were lower than today's, although how much lower is debated. Here, we use concentrations of iodate (the oxidized iodine species) in shallow-marine carbonate rocks (limestones and dolostones)—a proxy sensitive to both local oxygen availability and the relative proximity to anoxic waters—to generate the first comprehensive record of Proterozoic near-surface marine redox conditions. To assess the validity of our approach, Neogene-Quaternary carbonates are used to demonstrate that diagenesis most often decreases carbonate-iodine contents and is unlikely to increase them. Despite the potential for diagenetic loss, maximum Proterozoic carbonate iodine levels are elevated relative to those of the Archean, particularly during the Lomagundi and Shuram carbonate carbon isotope excursions of the Paleo- and Neoproterozoic, respectively. For the Shuram specifically, comparisons to Neogene-Quaternary carbonates suggest that diagenesis is not responsible for the observed iodine trends. The predominantly low iodine levels of Proterozoic carbonates relative to the Phanerozoic are most parsimoniously linked to a shallow oxic-anoxic interface, with O_2 concentrations in overlying surface water that were at least intermittently above the threshold required to support complex life. However, the diagnostically low iodine data from mid-Proterozoic shallow-water

carbonates relative to those of the bracketing time intervals suggest shallow and dynamic anoxic waters that episodically mixed upward and laterally, resulting in weakly oxygenated surface waters. This redox instability may have challenged early eukaryotic diversification and expansion, creating an evolutionary landscape unfavorable for the emergence of animals.

1. Introduction

The shallow oceans of the Proterozoic Eon were the host to both oxygen production and the sequential radiations of eukaryotes and animals (Knoll, 2014). Nevertheless, the current conversation about the oxygenation of the biosphere, the first appearances and diversification of the earliest eukaryotes and animals, and their associated oxygen demands (Mills et al., 2014; Sperling et al., 2013) has often focused instead on conditions in the atmosphere (Planavsky et al., 2014) and sub-photic deep-marine waters (Sperling et al., 2015). Such comparisons are indirect, since *in situ* oxygenic photosynthesis in the shallow photic zone provides the potential for elevated shallow-ocean oxygen at micromolar (μM) levels even under an anoxic atmosphere (Reinhard et al., 2016). This disconnect reflects a shortage of temporally expansive paleoredox records specific to the shallow ocean. The need to fill this knowledge gap is particularly critical through the mid-Proterozoic (ca. 1.8 to 0.8 billion years ago or Ga), which precedes the evolution of the earliest metazoans (Knoll, 2014).

Chromium isotope data have recently yielded estimates for atmospheric O_2 during the mid-Proterozoic as low as < 0.1-1% of present atmospheric levels (PAL), in contrast to previous estimates of >1-40% of PAL (Gilleaudeau et al., 2016; Planavsky et al., 2014). If these low estimates are correct, the predicted nanomolar (nM) to low μM equilibrium-driven levels of dissolved O_2 in the surface ocean would challenge most complex life (Planavsky et al., 2014; Reinhard et al., 2016). Generally consistent with low atmospheric pO_2 through portions of the Proterozoic, however, accumulations of redox-sensitive metals (Mo, Cr, U, and Fe) in basinal black shale specifically fingerprint an anoxic deeper ocean dominated by a combination of ferruginous and sulfidic (euxinic) waters (Gilleaudeau and Kah, 2015; Reinhard et al., 2013; Sperling et al.,

2015). Uncertainties about relationships among the atmosphere, deep ocean, and surface waters elevates the need for proxy perspectives specific to the shallowest layers of the ocean.

Ratios of iodine-to-calcium-magnesium, or I/(Ca+Mg), in shallow-marine carbonates can track the presence or absence of O_2 in the shallow ocean (Hardisty et al., 2014) and the position of the oxic-anoxic interface in the water column relative to the site of carbonate precipitation (Lu et al., 2016). The oxidized and reduced iodine species, iodate (IO_3^-) and iodide (I^-), respectively, constitute the bulk of total dissolved iodine in seawater (Chance et al., 2014; Emerson et al., 1979; Farrenkopf and Luther III, 2002; Rue et al., 1997; Wong and Brewer, 1977). Concentrations of total dissolved iodine in modern seawater, near 450-500 nM (Chance et al., 2014), are globally uniform and have a residence time (~300 kyrs) that is orders of magnitude longer than the mixing time of the ocean. Importantly, IO_3^- exists exclusively in oxic waters, with IO_3^- reduction occurring in weakly oxic waters prior to the onset of iron and sulfate reduction (Fig. 1; Emerson et al., 1979; Farrenkopf and Luther III, 2002; Kennedy and Elderfield, 1987a; Kennedy and Elderfield, 1987b; Rue et al., 1997; Wong and Brewer, 1977). Quantitative IO_3^- reduction is observed within anoxic basins (Emerson et al., 1979; Wong and Brewer, 1977) and in reducing pore waters (Kennedy and Elderfield, 1987a; Kennedy and Elderfield, 1987b). The redox behavior of iodine can be traced for ancient oceans because IO_3^- is the sole iodine species that co-precipitates with carbonate rocks (Lu et al., 2010). Thus, carbonate minerals formed in these anoxic waters—where I^- is the predominant dissolved iodine species—are not expected to incorporate iodine during precipitation, as demonstrated in calcite synthesis experiments (Lu et al., 2010). This expectation is consistent with previous reports noting a lack of iodine in carbonate rocks prior to the Great Oxidation Event (GOE) (Hardisty et al., 2014).

Although quantitative reduction of IO_3^- occurs within hours in low-oxygen and anoxic waters (Farrenkopf et al., 1997), I^- oxidation can be a slower process, with rate estimates ranging from weeks to years (Chance et al., 2014; Luther III et al., 1995). Due to this redox asymmetry, the

largest gradients in marine IO_3^- concentrations occur within the oxycline of oxygen minimum zone (OMZs) or anoxic basins (Fig. 1; Farrenkopf and Luther III, 2002; Rue et al., 1997). In this zone, weakly oxic conditions allow for IO_3^- accumulation, while *ex situ* input of the relatively slow oxidizing I^-—transported from underlying waters characterized by IO_3^- reduction—results in steep [IO_3^-] gradients (Farrenkopf and Luther III, 2002; Lu et al., 2016; Rue et al., 1997; Wong and Brewer, 1977). Modern seawater non-zero [IO_3^-] values of <250 nM are almost exclusively found in such settings (Fig. 1; Chance et al., 2014; Lu et al., 2016). This low range of seawater [IO_3^-] would be recorded as I/[Ca+Mg] ratios of < ~2.6 μmol/mol in carbonate, as observed in both laboratory calcite-precipitation experiments (Lu et al., 2010) and direct measurements of modern carbonate from low oxygen settings (Glock et al., 2014; Lu et al., 2016). Analogous to the oxyclines of modern OMZs and anoxic basins, ancient carbonate with non-zero I/(Ca+Mg) of less than ~2.6 μmol/mol are interpreted to reflect precipitation within waters with local O_2 levels above those necessary to sustain IO_3^- accumulation but which are also characterized by or in frequent exchange with waters hosting active IO_3^- reduction (Lu et al., 2016).

Importantly, diagenetic effects on I/(Ca+Mg) ratios have not been examined in previous studies. However, given that carbonate diagenetic mineral transformations occur most often in anoxic pore fluids marked by IO_3^- reduction (Loyd et al., 2012; McClain et al., 1992; Schrag et al., 2013), carbonate phases are expected to be particularly sensitive to diagenetic iodine loss. Carbonates of the Proterozoic Eon host the largest positive and negative $\delta^{13}C_{carb}$ excursions in Earth history—the Paleoproterozoic Lomagundi and Ediacaran Shuram anomalies, respectively. Although differing in direction, both have been interpreted as large-scale Proterozoic oxidation events bracketing the overall mid-Proterozoic low oxygen atmosphere (Fike et al., 2006; Lyons et al., 2014). However, these records are at best only indirect measures of redox conditions in the surface ocean, and their relationships to the broader workings of the carbon cycle as manifested in marine water column signals can be lost or overprinted during diagenesis by pore fluid chemistry (Schrag et al., 2013; Swart and Kennedy, 2012). If the effects of diagenesis on I/(Ca+Mg) are

116 understood, examination of I/(Ca+Mg) through Proterozoic carbon isotope excursions may provide
117 a means of testing whether these records represent pore fluid or water column chemistry.
118 Here we provide the first comprehensive record of Proterozoic surface ocean redox,
119 specifically tracking temporal marine IO_3^- availability through a compilation of I/(Ca+Mg) ratios
120 from mostly shallow-marine carbonate rocks (limestones and dolostones). This data set includes
121 carbonates capturing the Shuram $\delta^{13}C_{carb}$ excursion. We also provide the first constraints on iodine
122 proxy expressions linked to diagenetic alteration of recent carbonates. Through comparisons of
123 dissolved iodine cycling in modern low-oxygen versus well-oxygenated marine waters, I/(Ca+Mg)
124 records from pristine modern carbonates from both redox end members, and diagenetic carbonates
125 from Neogene-Quaternary settings, we suggest that oxygenation in the surface ocean following the
126 GOE was sufficient to sustain eukaryotic life. At the same time, we provide evidence against
127 diagenesis as a driver of the Shuram excursion. However, we further propose that the low
128 I/(Ca+Mg) ratios typical of the mid-Proterozoic reflect carbonate precipitation in waters with
129 overall low and unstable oxygen levels in close spatial proximity to anoxic waters.

130 **2. Materials**

131 To evaluate the effects of diagenetic mineral transformations on I/(Ca+Mg) ratios, we
132 include a series of Neogene-Quaternary case studies to provide a comprehensive view of initial
133 iodine precipitation and subsequent modification as a function of varying primary carbonate
134 mineralogy, carbonate burial history, and related diagenetic pathways—specifically, meteoric
135 diagenesis, marine burial diagenesis, and dolomitization. The case studies are outlined below (along
136 with citations to detailed previous studies of the same localities or samples), in Table 2, and in the
137 Supplemental Materials:

138 (1) **Short (ca. <16 cm) bank-top cores from the modern Great Bahama Bank, or GBB**
139 **(**Romaniello et al., 2013; Zhang et al., Accepted**).** These samples capture initial iodine

deposition in primary carbonates from a range of settings and primary mineralogies near Little Darby and Lee Stocking islands (Table 3; Supplementary Fig. 1 and 2).

(2) ***Montastrea annularis*** **coral heads from the Pleistocene Key Largo Limestone, south Florida**. This sample set includes aragonite-to-low-Mg calcite (LMC) transitions driven by subaerial exposure and subsequent diagenesis in meteoric pore waters. Post-depositional organic matter remineralization during aragonite-to-calcite neomorphism has resulted in negative $\delta^{13}C_{carb}$ in some of the LMC samples (Gill et al., 2008).

(3) **The Neogene-Quaternary Clino and Unda cores, Great Bahama Bank.** These cores were drilled ~8 km apart along the western edge of the Great Bahama Bank (Supplementary Fig. 1). The Clino core contains a negative $\delta^{13}C_{carb}$ excursion in the upper portion reflecting multiple periods of subaerial exposure and subsequent aragonite-to-calcite neomorphism in meteoric pore fluids (still ongoing at the top of the core), along with intervals with aragonite-to-calcite neomorphism occurring exclusively in marine pore fluids and minor dolomite, which were all sampled in detail (Melim et al., 1995; Swart and Melim, 2000; Swart and Kennedy, 2012). The Unda and Clino cores have similar depositional histories; however, for the purposes of this study, we did not sample the Unda core in the same stratigraphic detail as the Clino core. For the Unda core, we specifically sampled two intervals with extensive dolomite that formed in marine pore fluids.

(4) **Dolomite concretions of the Miocene Monterey Formation, California.** These samples represent dolomite derived mainly from alkalinity production and authigenic carbonate precipitation during remineralization of organic carbon in marine pore fluids, in contrast to neomorphism of carbonate precursors (Loyd et al., 2013).

With the exception of the Monterey Formation, the waters that hosted primary carbonate precipitation are constrained to have been well oxygenated, which implies that presently low and dramatically varying I/(Ca+Mg) ratios do not record shifts in the IO_3^- content of the local waters of

deposition. Instead, potential low I/(Ca+Mg) values or variations likely track secondary processes related to depositional setting, mineralogy, and related diagenetic overprinting of primary values.

We also measured I/(Ca+Mg) ratios of carbonate rocks (n=518) from 20 sedimentary successions spanning the late Paleoproterozoic to late Neoproterozoic (Table 1) and combined these results with previously published data (Glock et al., 2014; Hardisty et al., 2014; Loope et al., 2013; Lu et al., 2016; Lu et al., 2010; Zhou et al., 2015; Zhou et al., 2014). Details regarding age, stratigraphy, and complementary geochemistry for the individual sections are included in the Supplementary Materials. This data set also includes new results from four previously studied carbonate sections that capture the Ediacaran Shuram negative $\delta^{13}C_{carb}$ anomaly: the Khufai Formation of the Sultanate of Oman (Osburn et al., 2015); the Doushantuo Formation of South China; the Johnnie Formation of Death Valley, USA; and the Clemente Formation of northern Mexico (Loyd et al., 2013). For this and the previously published Precambrian iodine data (Hardisty et al., 2014), emphasis was placed on carbonate successions with independent sedimentological evidence for shallow-marine deposition and units with clear indications of secondary alteration, such as veins and metamorphism above greenschist grade, were avoided.

3. **Methods**

Iodine-to-calcium-magnesium ratios and magnesium-to-calcium ratios were measured at Syracuse University using a Bruker M90 quadrupole inductively-coupled-plasma mass spectrometer (ICP-MS) and at the University of California, Riverside, using a Agilent 7900c ICP-MS, according to standard methods (Hardisty et al., 2014; Lu et al., 2016; Lu et al., 2010; Zhou et al., 2015; Zhou et al., 2014). All samples from the Clino and Unda cores and the Monterey and Tieling formations were measured at UC Riverside and the remainder at Syracuse University. Approximately 3-5 mg of powdered carbonate was used for each analysis. Samples were sonicated in 1 mL DI water that was then centrifuged and decanted. Following this, 3% HNO_3 was added to each sample allowing for complete dissolution of all carbonate, and these were similarly sonicated

for ~10 minutes and centrifuged. The supernatant was diluted in a matrix with combinations of nitric acid and an iodine-stabilizing solution (tertiary amine or tetramethyl ammonium hydroxide) to obtain Ca concentrations of approximately 50 ppm. Calibration standards were made fresh each day from powdered potassium iodate in a similar matrix with the addition of 50 ppm Ca. The coral standard JCP-1 was analyzed intermittently with average values at Syracuse University and UC Riverside that were identical within error.

The mineralogical determinations for the Clino and Unda cores, Monterey, Key Largo, and Bahamas Bank top cores were performed at the University of Miami using a Panalytical X-Pert Pro via a method published previously (Melim et al., 1995). The associated error is ± 2 wt. %. Carbon and oxygen isotope values for the Johnnie Formation, the Clino and Unda cores, and portions of the GBB short cores were measured at the University of California, Riverside, using a GasBench II interface coupled, via continuous flow, to a Delta V Thermo Advantage IRMS (Isotope Ratio Mass Spectrometer). Carbon and oxygen isotope values for the C1, C4, C6, and C7 Bahamas Bank top cores were analyzed at The Center for Stable Isotope Biogeochemistry at UC, Berkeley, using a MultiCarb system connected with a GV IsoPrime mass spectrometer in dual inlet mode. Carbon and oxygen isotopes for the Doushantuo Formation were measured at the University of Nevada, Las Vegas, using a Kiel IV carbonate device connected to a Finnigan Delta V Plus mass spectrometer in dual inlet mode. All values are presented in the standard delta notation as per mil (‰) deviation from Vienna Pee Dee Belemnite (V-PDB), with replicate standard analyses yielding standard deviations typically better than 0.10 ‰ for carbon and oxygen isotopes.

4. Results

The highest I/(Ca+Mg) values in our Neogene-Quaternary samples, ranging from 6.0-11.6 μmol/mol, are found in predominantly aragonite and HMC samples from bank-top cores from the well-oxygenated GBB (Table 3; Fig. 4). The Key Largo coral heads contain I/(Ca+Mg) values that show little change across the meteoric fluid-driven aragonite-to-calcite mineralogy transition, with

only KL-11 containing samples with decreased iodine contents in some, but not all, LMC-dominated samples. The carbon and oxygen isotopic and mineralogical trends and values within specific intervals are generally consistent with that of previous work of different samples from the same core (e.g., Melim et al., 1995; Swart and Melim, 2000; Swart and Kennedy, 2012), including the negative $\delta^{13}C_{carb}$ excursion characterizing the meteoric zone in the Clino core (Fig. 3). The Clino core contains I/(Ca+Mg) ranging from below detection to 5.71 μmol/mol. The highest I/(Ca+Mg) values overlap with intervals containing relatively higher aragonite content, with most LMC- and dolomite-dominated intervals generally containing relatively lower I/(Ca+Mg) ratios. The Unda and Monterey samples have I/(Ca+Mg) values ranging from below detection to 0.46 and 1.01 μmol/mol, respectively. Of the samples containing greater than 20 wt.% dolomite, I/(Ca+Mg) ratios are < 0.46 and 0.40 μmol/mol for the Monterey Formation and the Unda core, respectively, with most values below detection.

Our Proterozoic samples contain both dolomite and limestone (Fig. 5), and iodine is present in some of the samples from nearly all the units evaluated (Fig. 6). Proterozoic I/(Ca+Mg) ratios from carbonates older than the late Ediacaran Shuram anomaly are ≤2.8 μmol/mol and are often much less—notably within the range observed in primary carbonate from modern low oxygen settings (yellow squares, Fig. 6). There is a drop in maximum I/(Ca+Mg) to ≤0.8 μmol/mol around ~2.0 Ga following the Lomagundi positive carbon isotope excursion (LE; ~2.2-2.1 Ga). In the following interval, from 2.0 to 1.0 Ga, maximum values of ≤0.8 μmol/mol are found in 13 of the 14 studied units with the only exception being the Tieling Formation of North China, where maximum I/(Ca+Mg) ratios are similar to those characterizing the LE and Neoproterozoic (Fig. 6). Starting at roughly 1.0 Ga, maximum values are more frequently elevated relative to the mid-Proterozoic. Lastly, all four of our Ediacaran, Shuram-age sections show a marked increase in I/(Ca+Mg) in phase with the dramatic decrease in $\delta^{13}C_{carb}$ (Fig. 7).

5. Discussion

5.1 Iodine behavior during Neogene-Quaternary carbonate diagenesis

241 Multiple previous studies have measured bulk iodine in ancient carbonate (Hardisty et al.,
242 2014; Loope et al., 2013; Zhou et al., 2015); however, published studies of modern carbonate iodine
243 contents have focused solely on calcitic foraminifera, and no study has measured carbonate iodine
244 contents within an independent framework of well-constrained diagenetic alteration. Below we
245 provide a context for interpreting our Proterozoic bulk carbonate data through a process-oriented
246 perspective that progresses from modern carbonate precipitation to deposition, burial, and
247 subsequent variable styles of diagenetic mineral transformations.

248 The highest I/(Ca+Mg) ratios in our Neogene-Quaternary sample set come from the GBB
249 bank-top cores (Table 3), which is the least altered sample set of this study and representative of
250 the carbonate iodine signature of initial deposition. The range in I/(Ca+Mg) values from bulk
251 aragonite-HMC in all the GBB bank-top core samples (6.0-11.6 μmol/mol; Table 3) is higher than
252 that found in LMC foraminifera, which in previous studies of well-oxygenated settings spans from
253 4-7 μmol/mol (Glock et al., 2014; Lu et al., 2016). None of our I/(Ca+Mg) profiles from any of the
254 seven GBB short cores increases with depth (Table 3; Supplementary Fig. 2), indicating that the
255 elevated I/(Ca+Mg) values are unrelated to post-burial processes. If we apply the partition
256 coefficients from laboratory LMC precipitation experiments (Lu et al., 2010; Zhou et al., 2014) to
257 the I/(Ca+Mg) ratios from our aragonite-HMC-dominated GBB carbonate, we predict local marine
258 IO_3^- abundance from ~600 nM to approaching 1 μM, which is not consistent with the typical range
259 observed in marine surface waters (roughly 300 to 450 nM; Chance et al., 2014). Uncertainties
260 surrounding partition coefficients for HMC and aragonite and potential vital effects associated with
261 uncharacterized skeletal debris may lead to errors in the estimated IO_3^- content of ambient waters.
262 However, the wide and elevated range in I/(Ca+Mg) from the GBB is not easily attributed to any
263 one factor, as the GBB I/(Ca+Mg) ratios differ even between adjacent oolitic shoals of similar
264 composition and show no clear covariation with mineralogy, $\delta^{13}C_{carb}$, or modern depositional
265 setting (Table 3; Supplementary Fig. 2). Regardless, our observations are consistent with previous
266 works indicating that the I/(Ca+Mg) ratios of primary carbonate minerals precipitated from well-

267 oxygenated seawater do not overlap with the 0-2.6 μmol/mol value observed for calcitic
268 foraminifera found within low oxygen settings (Lu et al., 2016). Variations above this 0-2.6
269 μmol/mol range should be interpreted with caution, if at all.

270 The Key Largo coral heads provide a case study specific to initial aragonite precipitation
271 and post-depositional meteoric aragonite-to-calcite neomorphism during subaerial carbonate
272 exposure (Gill et al., 2008). In this case, the I/(Ca+Mg) ratios of primary aragonite fall within the
273 range reported for LMC foraminifera from well-oxygenated settings (Fig. 2). Previous work from
274 these same samples has shown that lower dissolved elemental abundances (e.g., S, Sr) in fresh
275 (meteoric) waters versus seawater, which is also true of iodine (Fehn, 2012), lead to decreases in
276 their concentrations in diagenetic LMC relative to primary aragonite (Gill et al., 2008). Opposite
277 of this expectation, however, the primary I/(Ca+Mg) ratios general change little across the
278 aragonite-to-calcite transitions of our samples. The only exception is a LMC interval directly at the
279 reaction front of KL-11 that contains lower I/(Ca+Mg) relative to the primary aragonite (Fig. 2),
280 but there are no discernable differences between these and other LMC samples with relatively
281 elevated I/(Ca+Mg). The maintenance of high, primary I/(Ca+Mg) ratios during meteoric
282 diagenesis in the Key Largo may represent a special case where oxic diagenetic conditions allowed
283 for the iodine content of the primary aragonite to buffer iodine contents of the diagenetic LMC.
284 Sulfate reduction is known to partially promote aragonite-to-calcite neomorphism during meteoric
285 diagenesis in the Bahamas (McClain et al., 1992)—conditions where iodine would be present
286 primarily as I^-. However, the $\delta^{34}S$ values of carbonate-associated sulfate (CAS) in both our original
287 aragonite and secondary calcite Key Largo samples are similar to those of Pleistocene/modern
288 seawater sulfate (Gill et al., 2008), arguing against substantial sulfate reduction during meteoric
289 diagenesis. Nonetheless, the Key Largo profiles support that I/(Ca+Mg) ratios have the potential to
290 be maintained but are unlikely to increase following deposition and neomorphism driven by
291 diagenesis in meteoric fluids.

The Clino core best illustrates the range in diagenetic zones and related geochemical and mineralogical variability possible from the GBB (Fig. 3, 4). The diagenetic zones reflect a temporal transition from a slope to a platform depositional setting during the Neogene-Quaternary, with a negative $\delta^{13}C_{carb}$ excursion in the upper portion due to multiple periods of subaerial exposure and subsequent aragonite-to-calcite neomorphism within meteoric fluids (Melim et al., 1995; Swart and Melim, 2000). Below this depth, aragonite-to-calcite neomorphism and minor dolomitization occurred exclusively in marine pore waters (Melim et al., 1995; Swart and Melim, 2000). The I/(Ca+Mg) ratios from the aragonite-HMC GBB short cores and aragonitic portions of the Key Largo Limestone are most like those expected for primary I/(Ca+Mg) ratios from the Bahamian Clino core (i.e., I/(Ca+Mg) > 3 μmol/mol). Indeed, although the Clino core sample set no longer contains intervals with 100% aragonite and has only sparse HMC, the samples with higher aragonite contents do generally contain the I/(Ca+Mg) ratios that are above those observed from low oxygen depositional settings (Fig. 3, 4a). However, the core shows clear diagenetic iodine loss in secondary LMC and dolomite phases, as most of the Clino core I/(Ca+Mg) ratios overlap with the <2.6 μmol/mol values observed from low oxygen marine settings. The ratios show no distinct trends with $\delta^{13}C_{carb}$, with regard to diagenetic zones, specific to lithology, or across the facies transitions (Fig. 3). Instead, the inferred decreases in I/(Ca+Mg) ratios during diagenesis in the Clino core are consistent with previous inferences for neomorphism of aragonite and HMC to LMC and dolomite in marine pore waters hosting significant sulfate reduction and closed to seawater exchange (Swart and Melim, 2000). Despite initial deposition in a well-oxygenated setting with temporally varying facies likely hosting a large array of high primary I/(Ca+Mg) ratios, we surmise that progressive diagenesis will ultimately decrease ratios to relatively low values within a small range for the entire core, including the currently high I/(Ca+Mg) values in the aragonitic intervals near the top and bottom of our sampled profile.

The samples from the Unda core and Monterey concretions were specifically selected to provide constraints on iodine contents in dolomites that are well constrained to have precipitated

318 within marine pore waters (Fig. 4b). Our samples from the Unda core contain 100% dolomite in
319 many cases, which previous studies have linked to reefal sediments that experienced aragonite-to-
320 LMC neomorphism prior to dolomitization (Swart and Melim, 2000). Dolomite concretions of the
321 Monterey Formation are not dominantly derived from neomorphism of primary marine carbonate.
322 Instead, they represent authigenic dolomite precipitated in phase with extensive pore water
323 alkalinity production during remineralization in organic-rich sediments marked by anoxic pore
324 fluids closed to exchange with seawater (Blättler et al., 2015; Loyd et al., 2012). Despite the very
325 different mechanisms of dolomite precipitation, the two diagenetic dolomite sample sets reveal
326 similar results, yielding the lowest I/(Ca+Mg) ratios of our entire diagenetic data set. Most values
327 are below detection, and the highest value is 0.46 μmol/mol. We suggest that the extremely low
328 values reflect multiple generations of diagenetic mineral transformation for dolomites of the Unda
329 core and anoxic diagenetic conditions in both cases. The simple presence of any iodine in some
330 Monterey dolomite samples may indicate minor contributions from neomorphism of primary
331 carbonate that initially contained some iodine. The low I/(Ca+Mg) values from both dolomite
332 sample sets are not likely to reflect differences in partition coefficients for dolomite relative to
333 LMC, as many Proterozoic dolomites from this study have high ratios relative to the Neogene
334 sample set (discussed in the next section; Fig. 5). Ultimately, our results reveal that dolomitization
335 of carbonate precursors and authigenic dolomite precipitation in marine pore fluids will
336 dramatically lower I/(Ca+Mg) ratios from those characteristic of primary carbonate formed in well-
337 oxygenated water columns. Without proper caution, low dolomite ratios could lead to
338 underestimation of IO_3^- and hence the O_2 availability of the overlying water column.

339 **5.2 Neogene-Quaternary perspectives on Proterozoic carbonate diagenesis**

340 Our proxy validation efforts with the Neogene-Quaternary samples indicate that I/(Ca+Mg)
341 ratios should not increase post-depositionally during diagenesis in reducing pore fluids. Given this
342 observation, the simple presence of iodine in ancient carbonate is a robust fingerprint of oxic

conditions. Again, 'false positives' are not anticipated and have not been observed in young sediments. Iodine's redox relationship distinguishes it from other common paleoredox proxies (e.g., Fe speciation, S isotopes and concentrations, and Mo and U concentrations), which specifically fingerprint local anoxic water columns and are most commonly applied to deeper basinal shales. These approaches are far less effective at characterizing local oxic conditions because of complicating factors, such as relationships to sedimentation rate and diagenetic controls that can be insensitive to the redox conditions in the overlying waters. Beyond the simple presence-absence of surface ocean O_2, detailed comparison of Proterozoic I/(Ca+Mg) trends to Neogene-Quaternary diagenetic carbonate and dolomite support that Proterozoic temporal trends may reflect seawater redox evolution, including relative changes in the depth of anoxic waters relative to that of carbonate precipitation, when interpreted with the appropriate caution. For instance, there are no known temporal variations in diagenesis that would cause the observed first-order, long-term patterns through the Precambrian and preferentially favor the diagnostic persistence of low maximum values during the mid-Proterozoic and the absence of iodine in Archean samples (Fig. 6).

An additional, valuable case study in our effort to distinguish seawater versus pore water origins for Proterozoic I/(Ca+Mg) signals comes from a comparison between the I/(Ca+Mg) trends spanning the Shuram negative $\delta^{13}C_{carb}$ anomaly (Fig. 7) and our sample set recording Neogene-Quaternary diagenesis (Fig. 4), most notably that linked to the negative $\delta^{13}C_{carb}$ values of the Clino core (Fig. 2). Both meteoric and marine diagenesis have been invoked to explain the extremely negative $\delta^{13}C_{carb}$ values of the Shuram anomaly and other negative Neoproterozoic $\delta^{13}C_{carb}$ excursions (Schrag et al., 2013; Swart and Kennedy, 2012), with values trending from +5 to -12‰ (Fig. 7). The meteorically driven negative $\delta^{13}C_{carb}$ excursion of the Clino core has specifically been invoked to suggest the possibility that ancient negative $\delta^{13}C_{carb}$ excursions are products of diagenesis rather than secular evolution of the global carbon cycle (Swart and Kennedy, 2012). If diagenetic, the Shuram $\delta^{13}C_{carb}$ data would most likely reflect post-depositional mineralogical

transformations and the associated low $\delta^{13}C$ of dissolved inorganic carbon produced in pore fluids during organic matter remineralization under anoxic or reducing subsurface conditions. Our iodine data from the Clino core and other Neogene-Quaternary sediments confirm that I/(Ca+Mg) values do not increase during diagenesis and show no relationship with $\delta^{13}C_{carb}$ (Fig. 2), as IO_3^- is quantitatively reduced under the anoxic conditions typical of diagenetic carbonate precipitation (Kennedy and Elderfield, 1987a; Kennedy and Elderfield, 1987b). In contrast, however, I/(Ca+Mg) ratios across the Shuram excursion, at each of our four paleogeographic localities, *increase* in parallel with *decreasing* $\delta^{13}C_{carb}$ and do so consistently despite variable mineralogy and sedimentary facies (Fig. 7). Notably, the maximum observed I/(Ca+Mg) ratios vary among the Shuram sections, which could be the result of spatially varying, redox-driven local water column IO_3^- concentrations or a range of secondary factors that can lower the values in different ways (see diagenesis discussion). Regardless, the observed stratigraphic increase in I/(Ca+Mg) at all four locations in phase with the lower, falling $\delta^{13}C_{carb}$ limb of the Shuram anomaly is opposite of the pattern expected with diagenesis (Fig. 2, 4). Collectively, these data support the likelihood that the Shuram anomaly at least partially captures local seawater availability of IO_3^- and is a primary $\delta^{13}C$ feature tracking trends, likely global, in seawater chemistry. A primary contribution to the Shuram anomaly is further braced by records of CAS (Kaufman et al., 2007; Loyd et al., 2013; Osburn et al., 2015), U concentrations (Zhao et al., 2016), detailed Ca-Mg-C isotope comparisons (Husson et al., 2015), and compound-specific $\delta^{13}C$ of organic carbon (Lee et al., 2015), all of which show trends counter to those expected from diagenetic alteration.

Lastly, dolomitization in Proterozoic samples is not necessarily a source of false secular trends or, more generally, a fingerprint of severely altered samples with no confidence of recording signals of primary ocean chemistry. Instead, previous workers have argued from a combination of retention of primary sedimentary fabrics (Fairchild et al., 1991; Kah, 2000; Tucker, 1982), geochemical data (Husson et al., 2015; Kah, 2000; Tucker, 1982) and petrographic evidence (Tucker, 1982; van Smeerdijk Hood et al., 2011) that many dolomites formed

395 penecontemporaneous with deposition in Proterozoic sediments, in open exchange with seawater,
396 and in some cases at or near the sediment-water interface. Although stoichiometrically disordered
397 dolomite is subject to continued maturity during diagenesis (Vahrenkamp and Swart, 1994), one
398 implication is that the relatively long-term stability of dolomite relative to other carbonate phases
399 could mean that early Proterozoic dolomite, even if replacive, may be a strong and even preferred
400 geochemical archive of ancient marine conditions relative to stratigraphically associated, limestone
401 subject to diagenetic alteration during neomorphism. A comparison of iodine data from our
402 Neogene diagenetic dolomite from the Bahamas and Monterey to Proterozoic samples further
403 reinforces the potential frequency and benefit of early Proterozoic dolomite and points to processes
404 regulating I/(Ca+Mg) other than dolomitization in some of our samples (Fig. 5). Specifically, the
405 highest I/(Ca+Mg) ratios from our Proterozoic carbonates are found often in dolomite—a trend
406 opposite to that seen in our Neogene samples. Late stage diagenetic processes, such as contact with
407 anoxic brines, provide an unlikely explanation for the elevated I/(Ca+Mg) ratios in our Proterozoic
408 dolomite (Derry, 2010), as these fluids would not support elevated IO_3^- contents. Given the early
409 redox sensitivity of IO_3^- reduction with declining $[O_2]$, our data reinforce the idea that in some cases
410 Proterozoic dolomite precipitation likely occurred near or at the sediment-water interface and hence
411 should record at least partial seawater signals (Fairchild et al., 1991; Kah, 2000; Tucker, 1982; van
412 Smeerdijk Hood et al., 2011).

413 Given the combination of observations here and in previous work, broad first-order
414 temporal trends in maximum I/(Ca+Mg) ratios are cautiously considered in discussions below as
415 records of shallow ocean redox evolution. We emphasize again that our combined diagenetic data
416 explicitly reveal that post-depositional increases in I/(Ca+Mg) are unlikely, and hence, if anything,
417 the maximum I/(Ca+Mg) value from a given section is a minimum estimate of local seawater IO_3^-
418 availability. While we are not linking I/(Ca+Mg) ratios to a specific seawater IO_3^- concentration,
419 we do maintain that the first-order trends over billions of years are difficult to attribute to secondary
420 effects.

5.3 Comparing the modern and Proterozoic dissolved marine iodine reservoir

Our temporal I/(Ca+Mg) record in Figure 6 suggests the likelihood of changes in marine IO_3^- concentrations through time. Modern settings indicate that the control responsible for the largest shifts in local marine IO_3^- concentration is the local redox state (Fig. 1; Emerson et al., 1979; Farrenkopf and Luther III, 2002; Rue et al., 1997; Wong and Brewer, 1977); however, changes in the size of the total marine dissolved iodine reservoir (both IO_3^- and I^-) could control IO_3^- concentrations if oxic conditions prevailed. We consider this possibility below.

The Precambrian iodine reservoir was likely large relative to today's or, more generally, that of the Phanerozoic as a whole due to the absence or limited role of algal primary production and burial in marine sediments during the Precambrian. Marine sediments and sedimentary rocks are estimated to host as much as ~96% of crustal iodine, with the remaining fraction present in the hydrosphere and igneous and metamorphic rocks (Muramatsu and Hans Wedepohl, 1998). Algae, particularly brown algae, host the largest iodine enrichments in any known natural material by orders of magnitude, ultimately contributing to iodine concentration in organic-rich sediments (Muramatsu and Hans Wedepohl, 1998), which is recycled back to the ocean during weathering, diagenesis, and subduction (Fehn, 2012; Lu et al., 2010). Importantly, the first fossil evidence for algae does not appear until the late Mesoproterozoic Era (reviewed in Knoll, 2014), and algal-derived sterane biomarkers—representing eukaryotes—do not support algae being dominant contributors to marine organic matter until the latest Proterozoic (e.g., Brocks et al., 2016; Luo et al., 2015). Relatively lower iodine sinks in both Proterozoic sedimentary organic matter and carbonate (Fig. 6) point to a likely larger Proterozoic seawater iodine reservoir relative to today. These observations imply that our trends of low I/(Ca+Mg) in the Precambrian relative to the modern are unlikely to reflect a smaller marine reservoir of total dissolved iodine or shifts in that pool but instead derive from lower marine IO_3^- concentrations at the site of carbonate precipitation as related primarily to local redox.

For the Shuram anomaly specifically, we speculate that the oxidation of algae-derived organic matter could drive a temporally isolated increase in the total dissolved marine iodine reservoir. Oxidation of organic matter, as suggested in previous studies (Fike et al., 2006), also provides a mechanism for the input of isotopically light DIC into the ocean to produce the negative $\delta^{13}C_{carb}$ characteristic of the Shuram excursion. For instance, simple mass balance calculations suggest that the input of DIC from organic carbon oxidation (with a $\delta^{13}C$ of -25 ‰) necessary to drive a whole-ocean -17‰ $\delta^{13}C$ excursion (equivalent to that often inferred for the Shuram anomaly) in the modern ocean would increase the total marine dissolved iodine reservoir by a factor of ~1.6 (using the typical algae I/TOC ratio of 10^{-4}). However, given that I/(Ca+Mg) tracks IO_3^- and not total iodine, it is unlikely that the Shuram increase in I/(Ca+Mg) is simply a product of an increase in the total marine iodine reservoir. For example, regardless of an increase in the total iodine reservoir, IO_3^- concentrations (and hence I/(Ca+Mg) ratios) would decrease (the opposite of what is observed) during the excursion if oxidation of reduced carbon acted to simultaneously expand anoxia (Lu et al., 2010; Zhou et al., 2015). We suggest instead that an increase in marine IO_3^- through the Shuram anomaly would also require an expansion of oxic settings in the shallow ocean. Supporting this, concentrations and S isotope data for CAS through the Shuram anomaly provide evidence for an increase in marine sulfate concentrations and hence a general expansion of oxidizing conditions (Fike et al., 2006; Kaufman et al., 2007; Loyd et al., 2013; Osburn et al., 2015). Importantly, however, our iodine data do not demand that an oxidation event driving the negative $\delta^{13}C_{carb}$ excursion was linked to deep ocean ventilation. Oxygenation may instead have been limited to near-surface settings. This assumed redox stratification is supported by decreased I/(Ca+Mg) ratios following the event and thus an inferred return to more reducing conditions in the ocean (Fig. 7c), geochemical studies supporting widespread anoxia before and after the excursion (e.g., Johnston et al., 2013; Sperling et al., 2015), as well as mass balance calculations highlighting the challenges of maintaining the oxidants necessary to drive the $\delta^{13}C$ excursion if reflective of the whole-ocean ventilation (Bristow and Kennedy, 2008). Explaining the origin of the Shuram $\delta^{13}C_{carb}$

excursions remains a challenge; however, future models should consider the growing evidence for spatiotemporally limited oxidation specific to shallow settings.

5.4 Proterozoic surface ocean redox

In light of our study of diagenetic effects in recent carbonates, the simple presence of iodine in most of the Proterozoic carbonate units we analyzed provides strong evidence for surface ocean [O_2] above the low threshold required for IO_3^- accumulation. Previous studies have argued for an [O_2] requirement of at least 1-3 µM for marine IO_3^- accumulation and the presence of carbonate-bound iodine (Hardisty et al., 2014). Further support for Proterozoic surface ocean [O_2] at or above low µM levels comes from the fossil evidence for the presence of eukaryotic microfossils in mid-Proterozoic oceans (Knoll, 2014), as well as from modeling efforts indicating the potential for single digit µM surface ocean O_2 concentrations from *in situ* oxygenic photosynthesis under even a completely anoxic atmosphere (Reinhard et al., 2016). Importantly, the >1-3 µM O_2 levels inferred for the Proterozoic surface ocean are above those predicted from equilibrium calculations, assuming the very low mid-Proterozoic atmospheric pO_2 suggested recently by Cr isotope measurements (Fig. 6; Gilleaudeau et al., 2016; Planavsky et al., 2014), Collectively, the two proxies may provide evidence for a disequilibrium between the atmosphere and surface ocean favored by *in situ* photosynthetic oxygen production in the shallow waters (Reinhard et al., 2016). Alternatively, the apparent discrepancy could reflect the uncertainties in our current understanding of modern iodine (Chance et al., 2014; Luther III et al., 1995) and chromium cycling (compare Gilleaudeau et al., 2016, and Planavsky et al., 2014).

I/(Ca+Mg) ratios also provide new constraints on the degree of mixing of near-surface oxic waters with shallow anoxic waters (Lu et al., 2016). Given the relatively low I/(Ca+Mg) ratios observed through most of the Proterozoic (Fig. 6), we suggest that the iodine record most strongly supports a weakly oxidized surface ocean with shallow anoxic waters near or within the surface ocean for most of the Proterozoic. In other words, Proterozoic surface ocean redox was analogous

to the oxycline of modern anoxic basins and OMZs (Fig. 1). These modern settings—where oxygen is locally present, but IO_3^- reduction is active in resident and/or adjacent exchanging water masses—are characterized by sustained IO_3^- accumulation but with diagnostically low concentrations and corresponding I/(Ca+Mg) ratios in the range observed throughout the Proterozoic (yellow squares, Fig. 6). That pattern manifests in a predominance of low I/(Ca+Mg) ratios during the Proterozoic interrupted only episodically by largely minor increases (Fig. 6) during some intervals previously described as oxygenation events, such as at the GOE (Lyons et al., 2014), the Lomagundi excursion (Fig. 6; Lyons et al., 2014), at 1.4 Ga (Mukherjee and Large, 2016), the Neoproterozoic broadly (Planavsky et al., 2014), and the Shuram anomaly specifically (Fike et al., 2006). Collectively, these trends suggest a history of protracted and dynamic oxygenation within a largely anoxic ocean (Reinhard et al., 2013; Sperling et al., 2015) through the Proterozoic—rather than a unidirectional rise.

We specifically link the generally low but non-zero mid-Proterozoic iodine values to an extremely shallow oxycline that facilitated direct advective exchange between weakly oxic surface waters and underlying or adjacent waters that were dominantly anoxic (Reinhard et al., 2013; Sperling et al., 2015). In such a setting, it is likely that both upward and lateral mixing of O_2-free waters frequently perturbed and intruded into already poorly oxygenated shallow ocean waters. Reinforcing this interpretation, mid-Proterozoic records of chromium isotopes (Planavsky et al., 2014), Mo and Cr concentrations (Reinhard et al., 2013), rare earth elements (Tang et al., 2016), Zn/Fe ratios (Liu et al., 2016), and CAS (e.g., Kah et al., 2004) all indicate limited mid-Proterozoic biospheric oxygenation. Together with independent evidence for mid-depth euxinia throughout the mid-Proterozoic based on iron speciation analysis of shale (Fig. 6), the upward and lateral mixing of anoxic waters into weakly oxygenated surface waters may also have resulted in frequent episodic incursions of hydrogen sulfide into particularly shallow settings.

6. Summary and implications for Proterozoic life

The Proterozoic iodine record provides a comprehensive window to oxygen dynamics that may have dominated ancient, marginal shallow-marine settings—the ecological hot spots that likely hosted the emergence and diversification of eukaryotes, including animals (Jablonski et al., 1983; Knoll, 2014). This conclusion highlights the value of I/(Ca+Mg) data relative to other Proterozoic paleoredox records that are specific to the atmosphere (Cr isotopes) or to anoxic conditions in deeper marine settings (trace metals and Fe mineral speciation in shales). The overarching trends in our dataset are not easily linked to diagenetic processes, and there is strong support for a primary origin of iodine records across the heavily discussed Shuram excursion.

Previous debate regarding the potential for redox controls on the timing of early animal evolution has focused on experimental and ecological analyses of animal physiology (Mills et al., 2014; Sperling et al., 2013) as related to indirect estimates of atmospheric pO_2 (Planavsky et al., 2014). The iodine data provide a more direct perspective, suggesting the possibility of a Proterozoic surface ocean that was at least intermittently hospitable to eukaryotes and that may have been at, near, or above the lower limits of oxygen required for small, simple (but not large and energetic) animals (Mills et al., 2014; Sperling et al., 2013). Critically, however, our data also support the likelihood that the marginal shelf settings in which early protistan and, later, animal fossils are found were characterized by low and variable O_2 conditions (Gilleaudeau and Kah, 2015) most analogous to those within the oxyclines directly overlying modern OMZs and within anoxic basins. We argue that these conditions were particularly common through the mid-Proterozoic, with weakly oxygenated shallow waters impacted frequently if not persistently by upward and lateral intrusion of abundant anoxic waters. Despite maximum shallow ocean [O_2] that was likely near the proposed thresholds for simple, early animals, such dynamic conditions could have challenged eukaryotic and, later, animal emergence and diversification during the mid-Proterozoic for at least a billion years (Johnston et al., 2012).

Author Contributions

DH, ZL, XZ and CD analyzed I/(Ca+Mg) ratios. AB, BG, CW, DH, GJ, LK, AK, SL, MO, NP and PS provided sample material or aided with fieldwork. DH designed the study and wrote the manuscript, with major contributions from ZL and TL. MO, NP and AB also provided essential input throughout. All authors discussed the results and commented on and approved manuscript submission.

Acknowledgments

TL, ZL, and DH thank NSF EAR-1349252. ZL further thanks OCE-1232620. DH and TL acknowledge further funding from a NASA Early Career Collaboration Award. TL, AB, NP, DH, and AK thank the NASA Astrobiology Institute. TL and NP received support from the Earth-Life Transitions Program of the NSF. AB acknowledges support from NSF grant EAR-05-45484 and an NSERC Discovery and Accelerator Grants. We also thank Peter Swart for providing the Unda and Clino drill cores, which was supported by NSF funding to PS.

References

Blättler, C.L., Miller, N.R., Higgins, J.A., 2015. Mg and Ca isotope signatures of authigenic dolomite in siliceous deep-sea sediments. Earth and Planetary Science Letters 419, 32-42.

Bristow, T.F., Kennedy, M.J., 2008. Carbon isotope excursions and the oxidant budget of the Ediacaran atmosphere and ocean. Geology 36, 863-866.

Brocks, J., Jarrett, A., Sirantoine, E., Kenig, F., Moczydłowska, M., Porter, S., Hope, J., 2016. Early sponges and toxic protists: possible sources of cryostane, an age diagnostic biomarker antedating Sturtian Snowball Earth. Geobiology 14, 129-149.

Chance, R., Baker, A.R., Carpenter, L., Jickells, T.D., 2014. The distribution of iodide at the sea surface. Environmental Science: Processes & Impacts.

Derry, L.A., 2010. A burial diagenesis origin for the Ediacaran Shuram–Wonoka carbon isotope anomaly. Earth and Planetary Science Letters 294, 152-162.

Emerson, S., Cranston, R.E., Liss, P.S., 1979. Redox species in a reducing fjord: equilibrium and kinetic considerations. Deep Sea Research Part A. Oceanographic Research Papers 26, 859-878.

Fairchild, I.J., Knoll, A.H., Swett, K., 1991. Coastal lithofacies and biofacies associated with syndepositional dolomitization and silicification (Draken Formation, Upper Riphean, Svalbard). Precambrian Research 53, 165-197.

Farrenkopf, A.M., Dollhopf, M.E., Chadhain, S.N., Luther III, G.W., Nealson, K.H., 1997. Reduction of iodate in seawater during Arabian Sea shipboard incubations and in laboratory

cultures of the marine bacterium< i> Shewanella putrefaciens</i> strain MR-4. Marine Chemistry 57, 347-354.

Farrenkopf, A.M., Luther III, G.W., 2002. Iodine chemistry reflects productivity and denitrification in the Arabian Sea: evidence for flux of dissolved species from sediments of western India into the OMZ. Deep Sea Research Part II: Topical Studies in Oceanography 49, 2303-2318.

Fehn, U., 2012. Tracing crustal fluids: Applications of natural ^{129}I and ^{36}Cl. Annual Review of Earth and Planetary Sciences 40, 45.

Fike, D.A., Grotzinger, J.P., Pratt, L.M., Summons, R.E., 2006. Oxidation of the Ediacaran ocean. Nature 444, 744-747.

Gill, B.C., Lyons, T.W., Frank, T.D., 2008. Behavior of carbonate-associated sulfate during meteoric diagenesis and implications for the sulfur isotope paleoproxy. Geochimica et Cosmochimica Acta 72, 4699-4711.

Gilleaudeau, G., Frei, R., Kaufman, A., Kah, L., Azmy, K., Bartley, J., Chernyavskiy, P., Knoll, A., 2016. Oxygenation of the mid-Proterozoic atmosphere: clues from chromium isotopes in carbonates.

Gilleaudeau, G.J., Kah, L.C., 2015. Heterogeneous redox conditions and a shallow chemocline in the Mesoproterozoic ocean: evidence from carbon–sulfur–iron relationships. Precambrian Research 257, 94-108.

Glock, N., Liebetrau, V., Eisenhauer, A., 2014. I/Ca ratios in benthic foraminifera from the Peruvian oxygen minimum zone: analytical methodology and evaluation as proxy for redox conditions. Biogeosciences Discussions 11, 11635-11670.

Hardisty, D.S., Lu, Z., Planavsky, N.J., Bekker, A., Philippot, P., Zhou, X., Lyons, T.W., 2014. An iodine record of Paleoproterozoic surface ocean oxygenation. Geology 42, 619-622.

Husson, J.M., Higgins, J.A., Maloof, A.C., Schoene, B., 2015. Ca and Mg isotope constraints on the origin of Earth's deepest δ13C excursion. Geochimica et Cosmochimica Acta 160, 243-266.

Jablonski, D., Sepkoski, J.J., Bottjer, D.J., Sheehan, P.M., 1983. Onshore-offshore patterns in the evolution of Phanerozoic shelf communities. Science 222, 1123-1125.

Johnston, D., Poulton, S., Goldberg, T., Sergeev, V., Podkovyrov, V., Vorob'eva, N., Bekker, A., Knoll, A., 2012. Late Ediacaran redox stability and metazoan evolution. Earth and Planetary Science Letters 335, 25-35.

Johnston, D.T., Poulton, S., Tosca, N., O'Brien, T., Halverson, G., Schrag, D., Macdonald, F., 2013. Searching for an oxygenation event in the fossiliferous Ediacaran of northwestern Canada. Chemical Geology 362, 273-286.

612 Kah, L.C., 2000. Depositional δ18O signatures in Proterozoic dolostones: constraints on seawater
613 chemistry and early diagenesis.

614 Kah, L.C., Lyons, T.W., Frank, T.D., 2004. Low marine sulphate and protracted oxygenation of
615 the Proterozoic biosphere. Nature 431, 834-838.

616 Kaufman, A.J., Corsetti, F.A., Varni, M.A., 2007. The effect of rising atmospheric oxygen on
617 carbon and sulfur isotope anomalies in the Neoproterozoic Johnnie Formation, Death Valley,
618 USA. Chemical Geology 237, 47-63.

619 Kennedy, H., Elderfield, H., 1987a. Iodine diagenesis in non-pelagic deep-sea sediments.
620 Geochimica et Cosmochimica Acta 51, 2505-2514.

621 Kennedy, H.A., Elderfield, H., 1987b. Iodine diagenesis in pelagic deep-sea sediments.
622 Geochimica et Cosmochimica Acta 51, 2489-2504.

623 Knoll, A.H., 2014. Paleobiological perspectives on early eukaryotic evolution. Cold Spring
624 Harbor perspectives in biology 6, a016121.

625 Lee, C., Love, G.D., Fischer, W.W., Grotzinger, J.P., Halverson, G.P., 2015. Marine organic
626 matter cycling during the Ediacaran Shuram excursion. Geology 43, 1103-1106.

627 Liu, X., Kah, L., Knoll, A., Cui, H., Kaufman, A., Shahar, A., Hazen, R., 2016. Tracing Earth's
628 O2 evolution using Zn/Fe ratios in marine carbonates. Geochemical Perspectives Letters 2, 24-34.

629 Loope, G.R., Kump, L.R., Arthur, M.A., 2013. Shallow water redox conditions from the
630 Permian–Triassic boundary microbialite: The rare earth element and iodine geochemistry of
631 carbonates from Turkey and South China. Chemical Geology 351, 195-208.

632 Loyd, S.J., Berelson, W.M., Lyons, T.W., Hammond, D.E., Corsetti, F.A., 2012. Constraining
633 pathways of microbial mediation for carbonate concretions of the Miocene Monterey Formation
634 using carbonate-associated sulfate. Geochimica et Cosmochimica Acta 78, 77-98.

635 Loyd, S.J., Marenco, P.J., Hagadorn, J.W., Lyons, T.W., Kaufman, A.J., Sour-Tovar, F., Corsetti,
636 F.A., 2013. Local $\delta^{34}S$ variability in 580Ma carbonates of northwestern Mexico and the
637 Neoproterozoic marine sulfate reservoir. Precambrian Research 224, 551-569.

638 Lu, Z., Hoogakker, B.A., Hillenbrand, C.-D., Zhou, X., Thomas, E., Gutchess, K.M., Lu, W.,
639 Jones, L., Rickaby, R.E., 2016. Oxygen depletion recorded in upper waters of the glacial
640 Southern Ocean. Nature Communications 7.

641 Lu, Z., Jenkyns, H.C., Rickaby, R.E., 2010. Iodine to calcium ratios in marine carbonate as a
642 paleo-redox proxy during oceanic anoxic events. Geology 38, 1107-1110.

643 Luo, G., Hallmann, C., Xie, S., Ruan, X., Summons, R.E., 2015. Comparative microbial diversity
644 and redox environments of black shale and stromatolite facies in the Mesoproterozoic Xiamaling
645 Formation. Geochimica et Cosmochimica Acta 151, 150-167.

646 Luther III, G.W., Wu, J., Cullen, J.B., 1995. Redox Chemistry of Iodine in Seawater: Frontier
647 Molecular Orbital Theory Considerations. Aquatic chemistry: interfacial and interspecies
648 processes 244, 135.

649 Lyons, T.W., Reinhard, C.T., Planavsky, N.J., 2014. The rise of oxygen in Earth/'s early ocean
650 and atmosphere. Nature 506, 307-315.

651 McClain, M.E., Swart, P.K., Vacher, H.L., 1992. The hydrogeochemistry of early meteoric
652 diagenesis in a Holocene deposit of biogenic carbonates. Journal of Sedimentary Research 62.

653 Melim, L.A., Swart, P.K., Maliva, R.G., 1995. Meteoric-like fabrics forming in marine waters:
654 implications for the use of petrography to identify diagenetic environments. Geology 23, 755-
655 758.

656 Mills, D.B., Ward, L.M., Jones, C., Sweeten, B., Forth, M., Treusch, A.H., Canfield, D.E., 2014.
657 Oxygen requirements of the earliest animals. Proceedings of the National Academy of Sciences
658 111, 4168-4172.

659 Mukherjee, I., Large, R.R., 2016. Pyrite trace element chemistry of the Velkerri Formation, Roper
660 Group, McArthur Basin: Evidence for atmospheric oxygenation during the Boring Billion.
661 Precambrian Research.

662 Muramatsu, Y., Hans Wedepohl, K., 1998. The distribution of iodine in the earth's crust.
663 Chemical Geology 147, 201-216.

664 Osburn, M.R., Owens, J., Bergmann, K.D., Lyons, T.W., Grotzinger, J.P., 2015. Dynamic
665 changes in sulfate sulfur isotopes preceding the Ediacaran Shuram Excursion. Geochimica et
666 Cosmochimica Acta 170, 204-224.

667 Planavsky, N.J., Reinhard, C.T., Wang, X., Thomson, D., McGoldrick, P., Rainbird, R.H.,
668 Johnson, T., Fischer, W.W., Lyons, T.W., 2014. Low Mid-Proterozoic atmospheric oxygen levels
669 and the delayed rise of animals. Science 346, 635-638.

670 Reinhard, C.T., Planavsky, N.J., Olson, S.L., Lyons, T.W., Erwin, D.H., 2016. Earth’s oxygen
671 cycle and the evolution of animal life. Proceedings of the National Academy of Sciences,
672 201521544.

673 Reinhard, C.T., Planavsky, N.J., Robbins, L.J., Partin, C.A., Gill, B.C., Lalonde, S.V., Bekker,
674 A., Konhauser, K.O., Lyons, T.W., 2013. Proterozoic ocean redox and biogeochemical stasis.
675 Proceedings of the National Academy of Sciences 110, 5357-5362.

676 Romaniello, S.J., Herrmann, A.D., Anbar, A.D., 2013. Uranium concentrations and 238 U/235 U
677 isotope ratios in modern carbonates from the Bahamas: Assessing a novel paleoredox proxy.
678 Chemical Geology 362, 305-316.

679 Rue, E.L., Smith, G.J., Cutter, G.A., Bruland, K.W., 1997. The response of trace element redox
680 couples to suboxic conditions in the water column. Deep Sea Research Part I: Oceanographic
681 Research Papers 44, 113-134.

682 Schrag, D.P., Higgins, J.A., Macdonald, F.A., Johnston, D.T., 2013. Authigenic carbonate and the
683 history of the global carbon cycle. Science 339, 540-543.

684 Sperling, E.A., Halverson, G.P., Knoll, A.H., Macdonald, F.A., Johnston, D.T., 2013. A basin
685 redox transect at the dawn of animal life. Earth and Planetary Science Letters 371, 143-155.

686 Sperling, E.A., Wolock, C.J., Morgan, A.S., Gill, B.C., Kunzmann, M., Halverson, G.P.,
687 Macdonald, F.A., Knoll, A.H., Johnston, D.T., 2015. Statistical analysis of iron geochemical data
688 suggests limited late Proterozoic oxygenation. Nature 523, 451-454.

689 Swart, P.K., Kennedy, M.J., 2012. Does the global stratigraphic reproducibility of $\delta^{13}C$ in
690 Neoproterozoic carbonates require a marine origin? A Pliocene–Pleistocene comparison. Geology
691 40, 87-90.

692 Swart, P.K., Melim, L.A., 2000. The origin of dolomites in Tertiary sediments from the margin of
693 Great Bahama Bank. Journal of Sedimentary Research 70, 738-748.

694 Tang, D., Shi, X., Wang, X., Jiang, G., 2016. Extremely low oxygen concentration in mid-
695 Proterozoic shallow seawaters. Precambrian Research.

696 Tucker, M.E., 1982. Precambrian dolomites: petrographic and isotopic evidence that they differ
697 from Phanerozoic dolomites. Geology 10, 7-12.

698 Vahrenkamp, V., Swart, P., 1994. Late Cenozoic dolomites of the Bahamas: metastable
699 analogues for the genesis of ancient platform dolomites. Dolomites: A Volume in Honour of
700 Dolomieu 21, 133-153.

701 van Smeerdijk Hood, A., Wallace, M.W., Drysdale, R.N., 2011. Neoproterozoic aragonite-
702 dolomite seas? Widespread marine dolomite precipitation in Cryogenian reef complexes.
703 Geology 39, 871-874.

704 Wong, G.T., Brewer, P.G., 1977. The marine chemistry of iodine in anoxic basins. Geochimica et
705 Cosmochimica Acta 41, 151-159.

706 Zhang, S., Henehan, M.J., Hull, P.M., Reid, R.P., Hardisty, D.S., Hood, A., Planavsky, N.J.,
707 Accepted. Environmental and biological controls on boron isotope ratios in shallow marine
708 carbonates. Earth and Planetary Science Letters.

709 Zhao, M.-Y., Zheng, Y.-F., Zhao, Y.-Y., 2016. Seeking a geochemical identifier for authigenic
710 carbonate. Nature Communications 7.

711 Zhou, X., Jenkyns, H.C., Owens, J.D., Junium, C.K., Zheng, X.Y., Sageman, B.B., Hardisty,
712 D.S., Lyons, T.W., Ridgwell, A., Lu, Z., 2015. Upper ocean oxygenation dynamics from I/Ca
713 ratios during the Cenomanian–Turonian OAE 2. Paleoceanography.

714 Zhou, X., Thomas, E., Rickaby, R.E., Winguth, A.M., Lu, Z., 2014. I/Ca evidence for upper
715 ocean deoxygenation during the PETM. Paleoceanography 29, 964-975.

Table 1. Approximate ages and number of samples for Proterozoic geologic units measured for I/(Ca+Mg) ratios in this study. References to ages and lithological descriptions can be found in the supplementary materials.

Table 2. Approximate ages and number of samples for Neogene-Quaternary geologic units measured for I/(Ca+Mg) ratios in this study. Also shown are the diagenetic conditions affecting mineralogy at each study site. The relevant previous publications providing lithological, geochemical, and diagenetic constraints are provided in the Supplementary Materials and in some cases in the main text. The citations are relevant to the exact same samples (KL and Monterey), cores (Clino, Unda), and sampling localities (LD and LS Islands) as the samples measured for I/(Ca+Mg) ratios in this study.

Table 3. Coordinates, water depth, and key depositional features, and mineralogy for cores from near Little Darby and Lee Stocking Islands, Bahamas. Mineralogy is shown in wt. % high-Mg calcite (HMC). None of the cores contained dolomite and only minor calcite was found in the cores, with HMC + aragonite > 93.52 wt. %, meaning the sediments mostly consist of aragonite. The detailed mineralogy, $\delta^{13}C_{carb}$, $\delta^{18}O_{carb}$, and I/(Ca+Mg) for each sample can be found in Supplementary Table 1. Also shown is the I/(Ca+Mg) surface-most value and range for each short core.

733 **Figure Legends**

734 **Fig. 1.** Water column dissolved [IO_3^-] and [O_2] from a vertical transect through the Peruvian OMZ
735 (Rue et al., 1997). The vertical dashed line highlights the range of [IO_3^-] (<250 nM) that is nearly
736 exclusively observed in settings within or below the oxycline of marine anoxic basins and OMZs
737 (Lu et al., 2016). The shaded box outlining this zone refers to the portion of the profile where
738 corresponding I/(Ca+Mg) ratios are anticipated to be <2.6 μmol/mol, which is discussed in the main
739 text.

740 **Fig. 2.** The **(a)** facies and lithology (vertical and slanted lines represent ramp paleo geometry; Swart
741 and Melim, 2000), **(b)** carbonate mineralogy (aragonite-dark grey; HMC-red, LMC-white;
742 dolomite-blue), **(c)** $\delta^{13}C_{carb}$, and **(d)** I/(Ca+Mg) ratios for core the Clino core of the Great Bahama
743 Bank. References to the lithological descriptions can be found in the supplementary materials.

744 **Fig. 3. (a)** I/(Ca+Mg) and **(b)** $\delta^{13}C_{carb}$ for transects from three aragonite-dominated to calcite-
745 dominated portions of **(c)** *Montastrea annularis* coral heads of the Pleistocene Key Largo
746 Limestone of south Florida. The samples and transects are the exact same as those use in Gill et al.
747 (2008). A picture of the KL-1 coral head and drilled transect is shown in part c, with the circles
748 representing discrete sampling locations. The transects are drilled at centimeter intervals across a
749 mineralogical transition from aragonite to calcite driven by subarial exposure and diagenesis in
750 meteoric pore fluids. The aragonite can be discerned by the lighter color and the calcite by the
751 darker color, with the reaction void occurring between KL1-3 and KL1-4.

752 **Fig. 4.** The composition of **(A)** primary aragonite and high-Mg calcite and **(B)** diagenetic dolomite
753 relative to I/(Ca+Mg) ratios for the diagenetic sample set described in the main text and shown in
754 the key. The horizontal dashed line is at an I/(Ca+Mg) of 2.6 μmol/mol, the threshold below which,
755 as discussed in the text, is characteristic of reducing marine settings (Glock et al., 2014; Lu et al.,
756 2016).

757 **Fig. 5.** Comparison of I/(Ca+Mg) to Ca/Mg for the Neogene dolomite-bearing sample sets relative
758 to the Proterozoic sample set from this and previous studies (Hardisty et al., 2014). The lower panel
759 shows the relative proportion of limestone versus dolomite for varying Ca/Mg ratios. Ca/Mg ratios
760 >80 are present in the sample sets, but not shown in order to emphasize the relevant trends.

761 **Fig. 6.** Compilation of proxy data distinguishing the redox state of the atmosphere, surface ocean,
762 and deeper ocean. Events specified in the text are labeled, including the period marked by the first
763 known major eukaryotic diversification (vertical gray bar Knoll, 2014). **Upper panel:** The secular
764 trends in atmospheric oxygen as discussed in recent compilations (Lyons et al., 2014; Planavsky et

al., 2014). Dashed lines in upper panel represent uncertainty due to a lack of quantitative constraints. **Middle panel:** $\delta^{13}C_{carb}$ (upper thick black line) and I/(Ca+Mg) (Glock et al., 2014; Hardisty et al., 2014; Loope et al., 2013; Lu et al., 2016; Lu et al., 2010; Zhou et al., 2015; Zhou et al., 2014). I/(Ca+Mg) ratios represent surface ocean redox conditions. Blue symbols on the right side represent samples from modern to recent settings with independent evidence for well-oxygenated water columns and lacking indicators of diagenetic overprinting. This includes foraminifera (Lu et al., 2016), aragonitic coral heads of the Key Largo Limestone of this study, and aragonite to HMC-dominated bulk carbonate from the modern Great Bahama Bank of this study. The yellow symbols correspond to modern foraminifers from within the oxycline of reducing settings (Glock et al., 2014; Lu et al., 2016). The square symbols indicate data representing I/Ca from calcitic foraminifers, equivalent to I/(Ca+Mg) in the case of calcite. **Bottom panel:** Generalized deep ocean redox redox, as inferred from previous works utilizing iron mineral speciation (Sperling et al., 2015). Red and purple boxes represents ferruginous and euxinic deep-marine waters, respectively.

Fig. 7. The $\delta^{13}C_{carb}$, I/(Ca+Mg) ratios, and stratigraphic profiles for Ediacaran successions capturing the Shuram anomaly. **(A)** Khufai Formation, Oman ($\delta^{13}C_{carb}$ from Osburn et al., 2015), **(B)** the Johnnie Formation, Death Valley, USA, **(C)** Clemente Formation, Northern Mexico ($\delta^{13}C_{carb}$ from Loyd et al., 2013), and **(D)** Doushantuo Formation, Siduping of South China. 1σ for I/(Ca+Mg) is equal to 0.2 μmol/mol (see Methods), twice the width of the data points. References to stratigraphic and paleogeographic details are in the Supplementary Materials.

Tables

Table 1.

Geologic Unit	Approximate Age (billions of years)	n
Wooly Dolomite, Australia	2.03	11
Snare Group, Canada	1.97	4
Taltheilei Formation, Canada	1.88	14
Duck Creek Formation, Australia	1.80	22
Paradise Creek Formation, Australia	1.65	10
Helena Formation, USA	1.45	9
Tieling Formation, China	1.44	45
Kaltasy Formation, Russia	1.43	12
Dismal Lakes Group, Canada	1.30	16
Mescal Formation, USA	1.26	4
Angmaat Formation, Canada	1.15	17
Atar and El Mreiti Groups, Mauritania	1.10	17
Sukhaya Tunguska Formations, Russia	1.04	7
Shaler Group, Canada	0.85	17
Akademikerbeen Group, Svalbard; Limestone-Dolomite Series, Greenland	0.83	36
Beck Springs Dolomite, USA	0.75	20
Khufai Formation, Sultanate of Oman	0.58	122
Johnnie Formation, USA	0.58	30
Clemente Formation, Mexico	0.58	31
Doushantuo Formation, China (Siduping)	0.64-0.58	74

Table 2.

Age	Location	Diagenetic Setting	n
modern	Little Darby and Lee Stocking Islands, Bahamas	initial deposition	57
Pleistocene	Key Largo Limestone, South Florida	initial deposition, meteoric	30
Neogene-Quaternary	Clino, Bahamas	meteoric, marine burial, dolomitization	151
Neogene-Quaternary	Unda, Bahamas	dolomitization	49
Miocene	Monterey Fm, Central California	dolomite concretions	24

Table 3.

Core	Coordinates	Water Depth (m)	Key Features	HMC (wt. %)	I/(Ca+Mg) (µmol/mol)	
					Surface	Range
C1	23°51'24.59"N 76°13'30.85"W	<1	intertidal	6.6-23.0	10.2	8.1-10.2
C3	23°51'24.68"N 76°13'33.25"W	<5	subtidal/*Thalassia testudinum* bed	15.2-25.6	7.6	6.7-7.6
C4, C6	23°46'11.21"N 76° 6'48.92"W	<10	subtidal/former ooid shoal/peloid rich/*Thalassia testudinum* bed	13.7-31.3; 8.1-26.5	10.0; 9.4	8.4-10.8; 7.7-9.4
C5	23°45'57.18"N 76° 8'3.00"W	<10	subtidal/active ooid shoal/ooid aggregates or grapestones	4.7-9.3	11.6	6.0-11.6
C7	23°46'10.78"N 76° 6'51.48"W	<10	subtidal/active ooid shoal/ooid aggregates or grapestones	4.3-10.3	7.2	6.7-7.5
C8	23°51'21.55"N 76°13'33.52"W	<2	subtidal/active ooid shoal/ooid aggregates or grapestones	8.8-24.1	8.2	6.3-8.2

Figures

Fig. 1

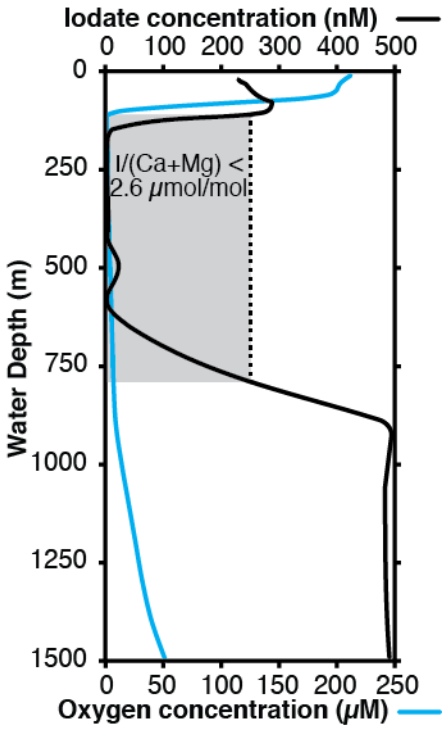

Fig. 2

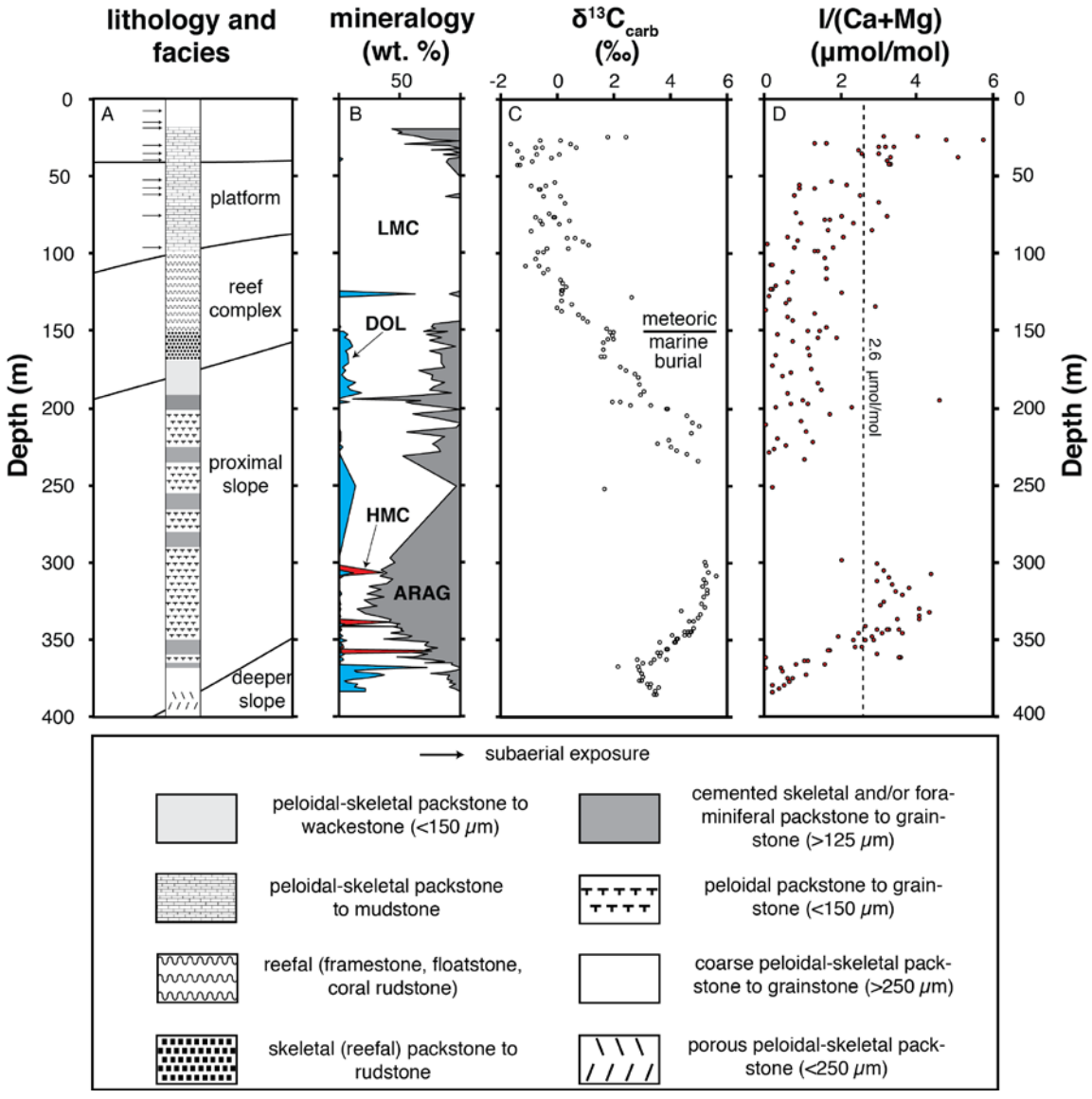
lithology and facies
mineralogy (wt. %)
δ13Ccarb (‰)
I/(Ca+Mg) (µmol/mol)
Depth (m)
A
B
C
D
platform
reef complex
proximal slope
deeper slope
LMC
DOL
HMC
ARAG
meteoric
marine
burial
2.6 µmol/mol
subaerial exposure
peloidal-skeletal packstone to wackestone (<150 µm)
peloidal-skeletal packstone to mudstone
reefal (framestone, floatstone, coral rudstone)
skeletal (reefal) packstone to rudstone
cemented skeletal and/or foraminiferal packstone to grainstone (>125 µm)
peloidal packstone to grainstone (<150 µm)
coarse peloidal-skeletal packstone to grainstone (>250 µm)
porous peloidal-skeletal packstone (<250 µm)

Fig. 3

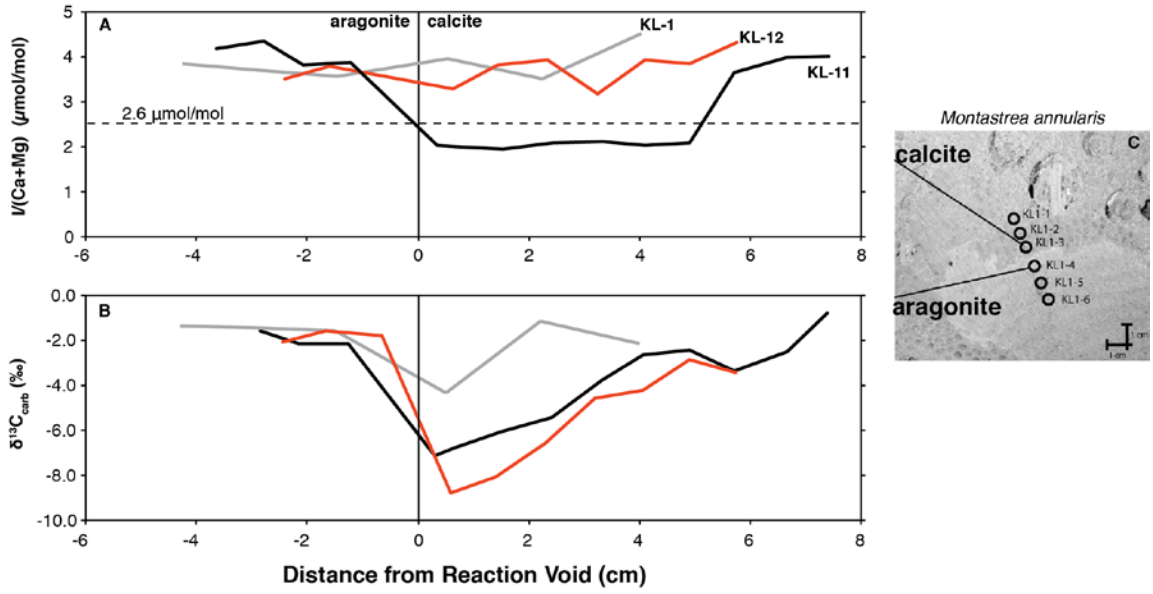
A
aragonite
calcite
KL-1
KL-12
KL-11
2.6 µmol/mol
Li/(Ca+Mg) (µmol/mol)
B
δ13Ccarb (‰)
Distance from Reaction Void (cm)
Montastrea annularis
C
calcite
aragonite
KL1-1
KL1-2
KL1-3
KL1-4
KL1-5
KL1-6

Fig. 4

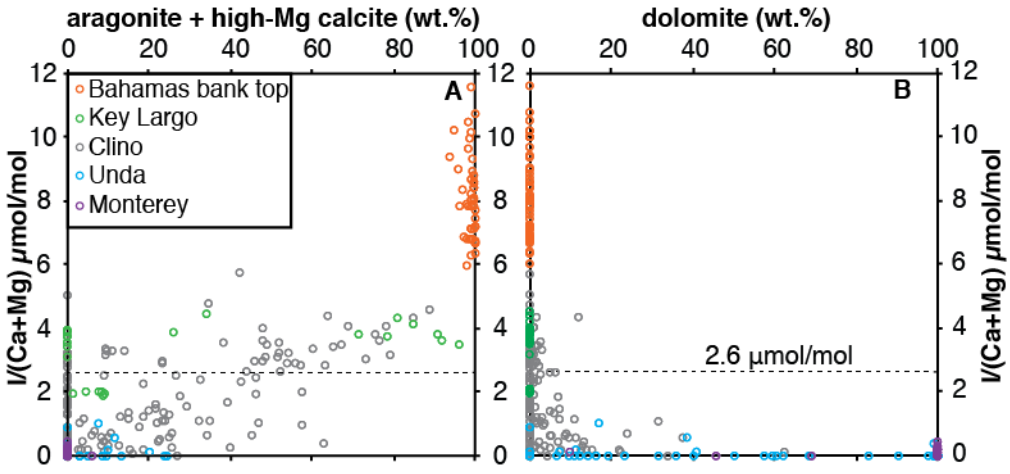
aragonite + high-Mg calcite (wt.%)
dolomite (wt.%)
I/(Ca+Mg) µmol/mol
Bahamas bank top
Key Largo
Clino
Unda
Monterey
A
B
2.6 µmol/mol

Fig. 5

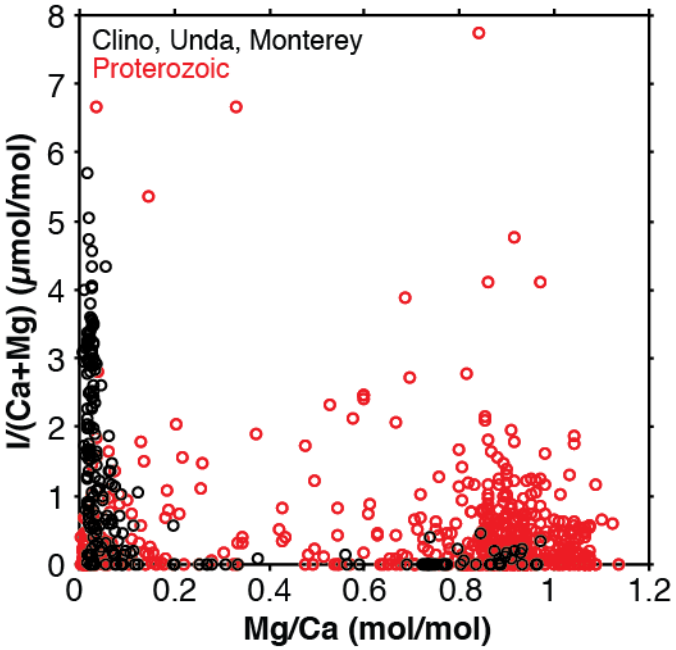
Clino, Unda, Monterey
Proterozoic
I/(Ca+Mg) (μmol/mol)
Mg/Ca (mol/mol)
0
1
2
3
4
5
6
7
8
0
0.2
0.4
0.6
0.8
1
1.2

Fig. 6

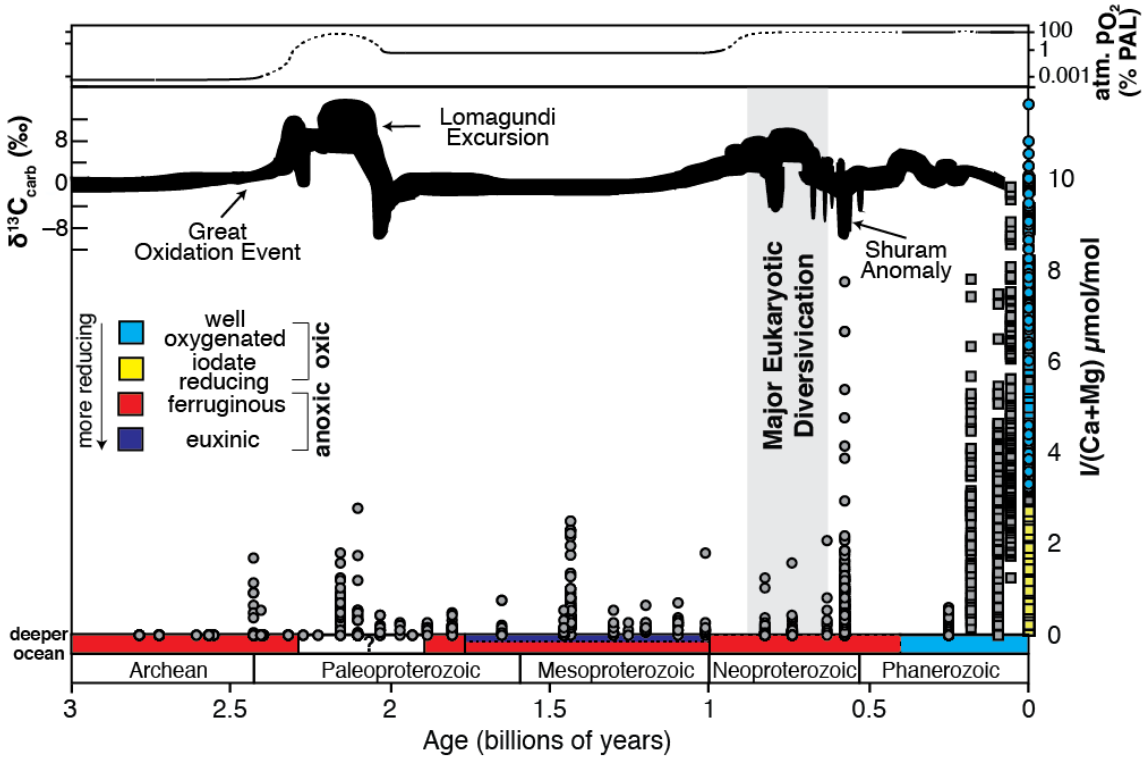
atm. PO_2 (% PAL)
100
1
0.001
$\delta^{13}C_{carb}$ (‰)
8
0
−8
Lomagundi Excursion
Great Oxidation Event
Shuram Anomaly
Major Eukaryotic Diversivication
I/(Ca+Mg) µmol/mol
10
8
6
4
2
0
more reducing
well oxygenated
iodate reducing
ferruginous
euxinic
oxic
anoxic
deeper ocean
?
Archean
Paleoproterozoic
Mesoproterozoic
Neoproterozoic
Phanerozoic
3
2.5
2
1.5
1
0.5
0
Age (billions of years)

Fig. 7

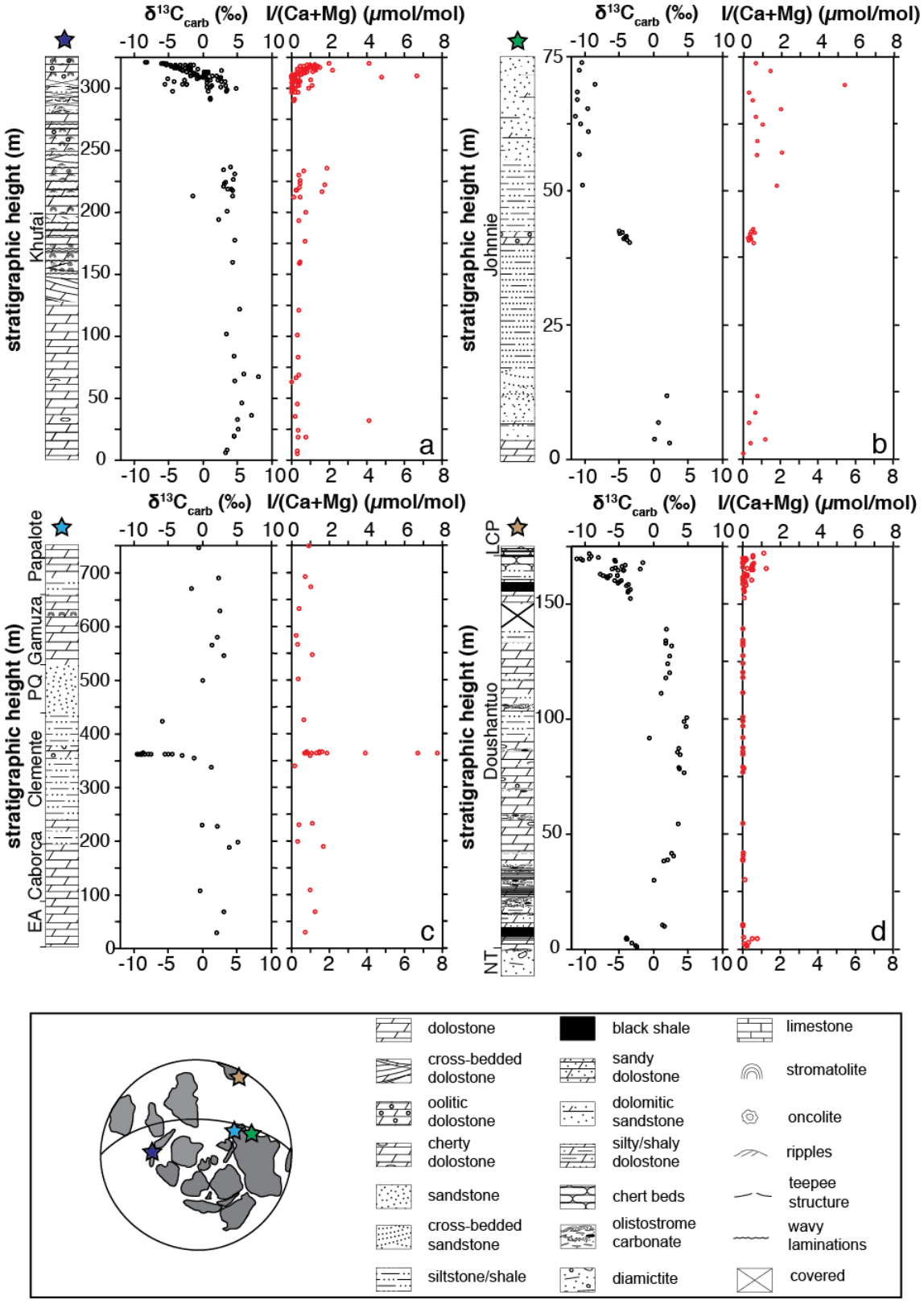
δ13Ccarb (‰)
I/(Ca+Mg) (μmol/mol)
stratigraphic height (m)
Khufai
Johnnie
Papalote
Gamuza
PQ
Clemente
Caborça
EA
Doushantuo
LCP
NT
a
b
c
d
dolostone
cross-bedded dolostone
oolitic dolostone
cherty dolostone
sandstone
cross-bedded sandstone
siltstone/shale
black shale
sandy dolostone
dolomitic sandstone
silty/shaly dolostone
chert beds
olistostrome carbonate
diamictite
limestone
stromatolite
oncolite
ripples
teepee structure
wavy laminations
covered